Monthly Notices
of the
ROYAL ASTRONOMICAL SOCIETY

MNRAS **445,** 4259–4266 (2014) doi:10.1093/mnras/stu2048

Millihertz quasi-periodic oscillations and broad iron line from LMC X-1

Md. Shah Alam,[1] G. C. Dewangan,[2] T. Belloni,[3] D. Mukherjee[2] and S. Jhingan[1]★

[1] *Centre for Theoretical Physics, Jamia Millia Islamia, New Delhi 110025, India*
[2] *Inter-University Centre for Astronomy & Astrophysics (IUCAA), Pune 411007, India*
[3] *INAF – Osservatorio Astronomico di Brera, Via E. Bianchi 46, I-23807 Merate, Italy*

Accepted 2014 September 27. Received 2014 September 19; in original form 2014 April 30

ABSTRACT

We study the temporal and energy spectral characteristics of the persistent black hole X-ray binary LMC X-1 using two *XMM–Newton* and a *Suzaku* observation. We report the discovery of low-frequency (∼26–29 m Hz) quasi-periodic oscillations (QPOs). We also report the variability of the broad iron Kα line studied earlier with *Suzaku*. The QPOs are found to be weak with fractional rms amplitude in the ∼1–2 per cent range and quality factor $Q \sim 2$–10. They are accompanied by weak red noise or zero-centred Lorentzian components with rms variability at the ∼1–3 per cent level. The energy spectra consist of three varying components – multicolour disc blackbody ($kT_{\rm in} \sim 0.7$–0.9 keV), high-energy power-law tail ($\Gamma \sim 2.4$–3.3) and a broad iron line at 6.4–6.9 keV. The broad iron line, the QPO and the strong power-law component are not always present. The QPOs and the broad iron line appear to be clearly detected in the presence of a strong power-law component. The broad iron line is found to be weaker when the disc is likely truncated and absent when the power-law component almost vanished. These results suggest that the QPO and the broad iron line together can be used to probe the dynamics of the accretion disc and the corona.

Key words: accretion, accretion discs – black hole physics – binaries: spectroscopic – stars: individual: LMC X-1 – X-rays: stars.

1 INTRODUCTION

The highly variable X-ray emission from black hole X-ray binaries (BHBs) shows a variety of quasi-periodic oscillations (QPOs) that appear as peaks of small but finite widths in the power density spectra (PDS; Remillard et al. 1999; Lewin & van der Klis 2006; Remillard & McClintock 2006; Belloni 2010; Motta et al. 2011). These QPOs can be grouped into three categories – (i) high-frequency QPOs that occur in the frequency range of ∼30–100 Hz and are generally transient (see e.g. Belloni, Sanna & Méndez 2012), (ii) low-frequency QPOs (LFQPOs) in the range of 0.05–30 Hz (Casella, Belloni & Stella 2005; Motta et al. 2011) and (iii) very low frequency (∼m Hz) QPOs that have been observed in the heartbeat sources GRS 1915+105 (Morgan, Remillard & Greiner 1997; Trudolyubov, Borozdin & Priedhorsky 2001) and IGR J17091−3624 (Belloni et al. 2000; Altamirano et al. 2011a). Recently, m Hz QPOs have also been detected from the BHBs H 1743−322 (∼11 m Hz; Altamirano & Strohmayer 2012) and IC X-1 (∼7 m Hz; Pasham & Strohmayer 2013). Some ultraluminous X-ray sources (ULXs) also show very low frequency QPOs at $\lesssim$100 m Hz, e.g. M82 X-1 (Strohmayer & Mushotzky 2003; Dewangan, Titarchuk & Griffiths 2006; Mucciarelli et al. 2006; Caballero-García, Belloni & Zampieri 2013; Pasham & Strohmayer 2013), NGC 5408 X-1 (Dheeraj & Strohmayer 2012), although they could be the counterpart of LFQPOs if these ULXs contain intermediate-mass black holes. The LFQPOs come in varieties with three main types – type A (weak with a few per cent rms and broad peak around 8 Hz), type B (relatively strong with ∼4 per cent rms and narrow peak around 6 Hz) and Type C (strong up to 16 per cent rms, narrow and variable peak) (see e.g. Casella et al. 2005).

While the exact origin of QPOs from BHBs is still a mystery, the type C LFQPOs are correlated with energy spectral properties. The centroid frequency is found to be correlated with the disc flux (Markwardt, Swank & Taam 1999; Motta et al. 2011), and the root-mean-square (rms) amplitude is found to increase with energy (Belloni et al. 1997; Casella et al. 2004; Belloni, Motta & Muñoz-Darias 2011). It implies that the LFQPOs do not directly arise from the thermal accretion disc as the accretion disc emission does not extend to higher energies.

The evolution of black hole transients can be characterized in terms of a limited number of states, namely Low hard state (LHS), hard intermediate state (HIMS), soft intermediate state (SIMS), high soft state (HSS) and the transitions between these states. The LHS is characterized by a strong dominant power-law emission with a

---

★ E-mail: sanjay.jhingan@gmail.com

Published by Oxford University Press on behalf of the Royal Astronomical Society

variable slope ($\Gamma \sim 1.5$–2.1) correlated with flux and a high-energy cutoff, also variable between 60 and 120 keV (see e.g. Motta, Belloni & Homan 2009). In the HIMS, a softer component originating from a thermal accretion disc component contributes more to the observed emission and the power-law component steepens, with an increase in the high-energy cutoff value (Motta et al. 2009; Belloni et al. 2011). The SIMS is softer than the HIMS due to larger contribution of the disc emission and is characterized by low level (∼a few per cent rms) of variability (Belloni et al. 2011). The LHS is usually associated with a steady radio jet (Corbel et al. 2013, and references therein). In the HIMS, a type C LFQPO is always observed, as is often the case in the brightest LHS. In the SIMS, QPOs of type A or B are often observed. In contrast, LFQPOs are generally not observed in the HSS dominated by thermal emission from accretion discs (see reviews by Remillard & McClintock 2006; Belloni 2010).

Hard X-ray irradiation of the thermal accretion disc can give rise to X-ray fluorescence emission lines below 10 keV and Compton reflection hump in the 10–50 keV band. The iron Kα emission line, broadened by Doppler and gravitational effects near a black hole in X-ray binaries and active galactic nuclei, is proven to be one of the most important diagnostic of the innermost regions of strong gravity (see e.g. Reynolds & Nowak 2003; Miller 2007). The strength and extent of the red wing of the relativistic iron line are determined by the inner extent of the accretion disc which is smaller than $6r_{\rm g}$ if the black hole is spinning, where $r_{\rm g} = GM/c^2$ is the gravitational radius. For a maximally spinning black hole, the innermost stable circular orbit is $r_{\rm ISCO} \sim r_{\rm g}$. Indeed, the presence of broad iron lines in the X-ray spectra of both BHBs and AGN has been used to determine the size of the inner disc and from that to infer the black hole spin.

The production of a broad iron line depends both on the presence of an accretion disc extending to the innermost regions and a strong hard X-ray continuum illuminating the disc. The presence of LFQPOs also depends on the power-law component. This suggests that the iron Kα line and LFQPOs are likely related, though not directly. In the soft spectral states, strong iron K lines are usually not observed, due to lack of strong hard X-ray continuum (Miller 2007). Similarly, LFQPOs are not observed in the high/soft states. The relationship between the broad iron line and the LFQPOs, their dependence on the hard X-ray continuum and the presence of an accretion disc are good tests of disc/corona geometry and the models for the origin of both the iron line and LFQPOs.

LMC X-1, located in the Large Magellanic Cloud, is a luminous and persistent BHB. It consists of a $10.19 \pm 1.41\,{\rm M}_{\odot}$ black hole primary and an O7 III companion orbiting each other with a 3.9 d period (Cowley et al. 1995; Orosz et al. 2009). The companion drives a strong wind that powers the black hole with an average luminosity of $0.16L_{\rm Edd}$ (Nowak et al. 2001; Gou et al. 2009). LMC X-1 has remained in the HSS persistently and has never been observed to undergo a transition to the LHS (Nowak et al. 2001; Ruhlen, Smith & Swank 2011). The temporal properties of LMC X-1 are typically of HSS with its PDS approximately proportional to ν^{-1} and fractional rms variability of ∼7 per cent (Nowak et al. 2001). Previously, two QPOs at 75 and 142 m Hz have been reported from LMC X-1, based on *Ginga* observations (Ebisawa, Mitsuda & Inoue 1989). However, a series of nine *RXTE* observations performed in 1996 (Schmidtke, Ponder & Cowley 1999) and a long 170 ks *RXTE* observation (Nowak et al. 2001) did not detect any QPO from the source. It has been suggested that the 75 and 142 m Hz QPOs detected by Ebisawa et al. (1989) are likely an artefact due to incorrect estimation of the Poisson noise level (Nowak et al. 2001). The X-ray spectrum of LMC X-1 is typical of the HSS in which the thermal disc component dominates over the power-law component (Ebisawa et al. 1989; Nowak et al. 2001; Ruhlen et al. 2011). However, spectral evolution of LMC X-1 does not follow the modified Stefan–Boltzmann relation $L_{\rm disc} \propto T_{\rm in}^4$ expected from the HSS of BHBs (see Ruhlen et al. 2011). The presence of a broad iron line from LMC X-1, earlier inferred from *RXTE* observations (Nowak et al. 2001), has been confirmed by Steiner et al. (2012) who measured a spin $a = 0.97^{+0.02}_{-0.025}$ using *Suzaku* observations. Steiner et al. (2012) also found a strong correlation between the relative strength of the Compton power law and the iron line flux using the *RXTE* observations.

In this paper, we perform timing and spectral study of LMC X-1 based on *XMM–Newton* and *Suzaku* observations and report the detection of m Hz QPOs and variable broad iron line. We show that the iron line and the QPO are not always present, and investigate the relationship between them. We describe the observations analysed and data reduction in Section 2, temporal analysis in Section 3 and spectral analysis in Section 4. We finally discuss our results in Section 5.

2 OBSERVATIONS AND DATA REDUCTION

2.1 *XMM–Newton*

XMM–Newton observed LMC X-1 twice: on 2000 October 21 (obsID: 0112900101, hereafter XMM-101) and 2002 September 26 (obsID: 0023940401, hereafter XMM-401) for exposure times of 7.2 and 40 ks, respectively. The EPIC-pn camera was operated in timing mode using the thick optical blocking filter in 2000 October and thin filter in 2002 September. The MOS cameras were operated in the full frame mode using the medium optical blocking filter in both observations. We used SAS version 12.0 and the most recent calibration data base to process and filter the event data. We corrected the EPIC-pn event list for the rate-dependent charge transfer inefficiency which has been seen in the fast mode data.[1] We checked for particle background by extracting light curves above 10 keV from both EPIC-pn and MOS data. No flaring background was found in the XMM-101 data. In the XMM-401 data, the flaring particle background was present in the beginning of observation for a short interval of ∼1400 s and after an elapsed time of ∼26 ks. We excluded these intervals of high particle background by using good time intervals created based on count rate cutoff criteria. We extracted the 10–12 keV light curve from the EPIC-pn data and created a GTI file by selecting the intervals with the count rate ≤ 0.5 counts s^{-1}. We then applied the GTI file and filtered the event list for high particle background. This resulted in the net exposures of 23.3 ks for the XMM-401 observation. The MOS data from both observations were affected with photon pile-up. So, we did not use MOS data for further analysis.

In the EPIC-pn timing mode, only one CCD chip is operated. The data are collapsed into one-dimensional row of size 64 pixels or 4.4 arcmin and are continuously transferred along the second dimension and readout at high speed resulting in 30 µs time resolution. This allows for high count rates and photon pile-up is negligible below 800 counts s^{-1}.[2] The EPIC-pn count rate of LMC X-1 was only 113 counts s^{-1}. Hence, the EPIC-pn data in the timing mode were not affected with pile-up which was also verified with `epatplot`. We extracted the source spectra from the EPIC-pn single

---

[1] http://xmm2.esac.esa.int/external/xmm_sw_cal/calib/index.shtml

[2] http://xmm.esac.esa.int/external/xmm_user_support/documentation/uhb_2.1/XMM_UHB.html

pixel events using a rectangular region of 15 pixel width covering the source. We also extracted the corresponding background spectra using two rectangular regions of widths 10 and 5 pixels away from the source. We used the SAS tasks `rmfgen` and `arfgen` to generate the response files.

2.2 *Suzaku*

Suzaku observed LMC X-1 starting on 2009 July 21, 18:38 UT for 129.8 ks (Observation ID 404061010). The observation was performed at XIS nominal pointing and the XIS were operated in the 1/4 window mode resulting in time resolution of 2 s. We used *Suzaku* FTOOLS version 19 and reprocessed and screened the XIS and HXD PIN data using the `aepipeline` and the most recent version of calibration data base to produce the cleaned event lists. We checked for photon pile-up in the XIS data using the ISIS tools[3] `aeattcor.sl` and `pile_estimate.sl`. A new attitude file was created which was then applied to the XIS event lists that resulted in sharper images. An estimated, minimum pile-up fraction image was created at different levels 0.03, 0.3, 1, 2, 5, 10 and 20 per cent. For spectral extraction from the XIS0 data, we made a circular region file with 130 arcsec radius and from its centre excluded a rectangular region (14.5 arcsec × 32.3 arcsec) with pile-up fraction >5 per cent. Similar regions were created for XIS1 and XIS3. The source spectra were extracted from these regions using XSELECT. We also extracted background spectra from multiple circular regions with typical sizes ∼60 arcsec away from the source. The response files were created using the tools `xisrmfgen` and `xissimarfgen`. The HXD/PIN spectral products were extracted using the tool `hxdpinxbpi`.

3 TEMPORAL ANALYSIS

We used the X-ray timing software GHATS[4] version 1.1.0 to compute PDS. We begin with temporal analysis of 0.3–10 keV *XMM–Newton* EPIC-pn data. The PDS for XMM-401 were created with a time bin size of 0.096 s (Nyquist frequency of 5.2 Hz), and time segments of 4096 bins in each light curve. The PDS of different segments were averaged and the resulting PDS were logarithmically rebinned in frequency to improve statistics. The PDS were computed using rms normalization (Belloni & Hasinger 1990). The PDS for the XMM-101 data were derived using a time resolution of 60 ms and time segments of 16 384 bins in each light curve. The averaged and logarithmically binned PDS for XMM-101 and XMM-401 are shown in Fig. 1. The PDS of LMC X-1 is featureless red noise during XMM-101 while a clear narrow peak in addition to the red noise is seen in the XMM-401 data.

The PDS were fitted using ISIS version 1.6.2-27. Unless otherwise specified, all errors on the best-fitting parameters are quoted at the 90 per cent confidence level corresponding to the minimum $\chi^2 + 2.71$. The detection significance of the QPOs was calculated based on the 1σ errors corresponding to the minimum $\chi^2 + 1.0$. A constant variability power results from Poisson noise alone; therefore, we first fitted a constant model to the PDS derived from the XMM-401 data. This model resulted in unsatisfactory fit (χ^2/dof = 161.5/91) with large residuals around ∼0.03 Hz. We then added a model for a Lorentzian-shaped QPO for the ∼0.03 Hz narrow feature. The parameters of the QPO model are the centroid frequency ($\nu_{\rm qpo}$), the quality factor ($Q = \nu_{\rm qpo}/\Delta\nu$) and the normalization (rms/mean). The CONSTANT+QPO model improved the fit to χ^2/dof = 97.4/88, and resulted in small residuals at the lowest frequencies below 0.006 Hz. Addition of a power-law component (PLAW) resulted only in marginal improvement (χ^2/dof = 91.2/86). The QPO is detected at a very high (6.8σ) statistical significance level, computed as the ratio between the best fitting normalization and its 1σ negative error. The best-fitting centroid frequency is $\nu_{\rm qpo} = 2.77^{+0.13}_{-0.12} \times 10^{-2}$ Hz and the quality factor $Q = \nu_{\rm qpo}/\Delta\nu = 3.8^{+3.2}_{-1.4}$. Without the PLAW component, the QPO is detected at much higher (15.2σ) significance level and the QPO parameters remained similar. For XMM-101, we found that the CONSTANT+PLAW model adequately describes the PDS (χ^2/dof = 106.3/106) without any requirement for a QPO. We calculated an upper limit on the rms of a possible QPO by adding a QPO model. We fixed the QPO frequency and the quality factor to the best-fitting values obtained for the XMM-401 data and varied the QPO normalization. This resulted in χ^2/dof = 106.3/105 and the 90 per cent upper limit on the fractional rms is 1.1 per cent.

To create the PDS of LMC X-1 using the *Suzaku* XIS data, we extracted light curves with 2 s bins from the XIS0, XIS1 and XIS3 cleaned data in the 0.4–9 keV band and combined the three light curves. We used the XRONOS task *powspec* to generate the PDS from the combined XIS light curve. We divided the light curve in 131 segments of 1024 bins. We discarded segments with gaps and calculated the PDS from each segment without any gap and averaged the power in each frequency bin and obtained the final PDS. We fitted the PDS in the 2.5 × 10^{-4}–0.25 Hz range derived from the *Suzaku*/XIS data. We used a broad Lorentzian, a power-law and a constant model for the continuum as it provided a better fit (χ^2/dof = 694.9/506) compared to the PLAW + CONSTANT (χ^2/dof = 725.9/509). Examination of the residual showed a narrow peak at ∼0.027 Hz, and addition of a QPO improved the fit to χ^2/dof = 671.8/503. Thus, we again detected a QPO at high significance (6.4σ level). The centroid of the QPO is almost at the same frequency ($\nu_{\rm qpo} \sim 0.027$) as for the XMM-401 data, and the coherence is high ($Q \sim$ 4–17). We have listed the best-fitting PDS parameters for the three observations in Table 1. We have shown the PDS data and the best-fitting models in the third row of Fig. 1. We also created EPIC-pn light curve folded with the corresponding QPO period using the FTOOLS task *efold*.

4 SPECTRAL ANALYSIS

We used ISIS version 1.6.2-27 for our spectral analysis. As before, we quote the errors on the best-fitting model parameters at the 90 per cent confidence level. In all spectral fits, we used the absorption model TBVARABS (Wilms, Allen & McCray 2000) with fixed abundances as obtained by Hanke et al. (2010).

We began with the spectral fitting of the broad-band *Suzaku* data. The broad-band spectrum of LMC X-1 extracted from the same data has been studied in detail by Steiner et al. (2012), who discovered the relativistic iron Kα line and measured the black hole spin $a_\star = 0.97^{+0.02}_{-0.25}$. Our purpose here is to study the spectral variability of LMC X-1 using *Suzaku* and *XMM–Newton* observations. We grouped the XIS spectral data to a minimum signal-to-noise of 10 and minimum channel of 2 in each bin. This ensures a minimum of more than 90 counts per bin. To check the cross-calibration issues between the three XIS instruments, we fitted an absorbed DISKBB plus POWERLAW model jointly to the XIS0, XIS1 and XIS3 data in the 0.5–10 keV band. Examination of the data to model ratio showed a discrepancy between the three XISs as large as 20 per cent below 2.5 keV. Therefore, we excluded XIS data

---

[3] http://space.mit.edu/CXC/software/suzaku/index.html

[4] http://astrosat.iucaa.in/∼astrosat/GHATS_Package/Home.html

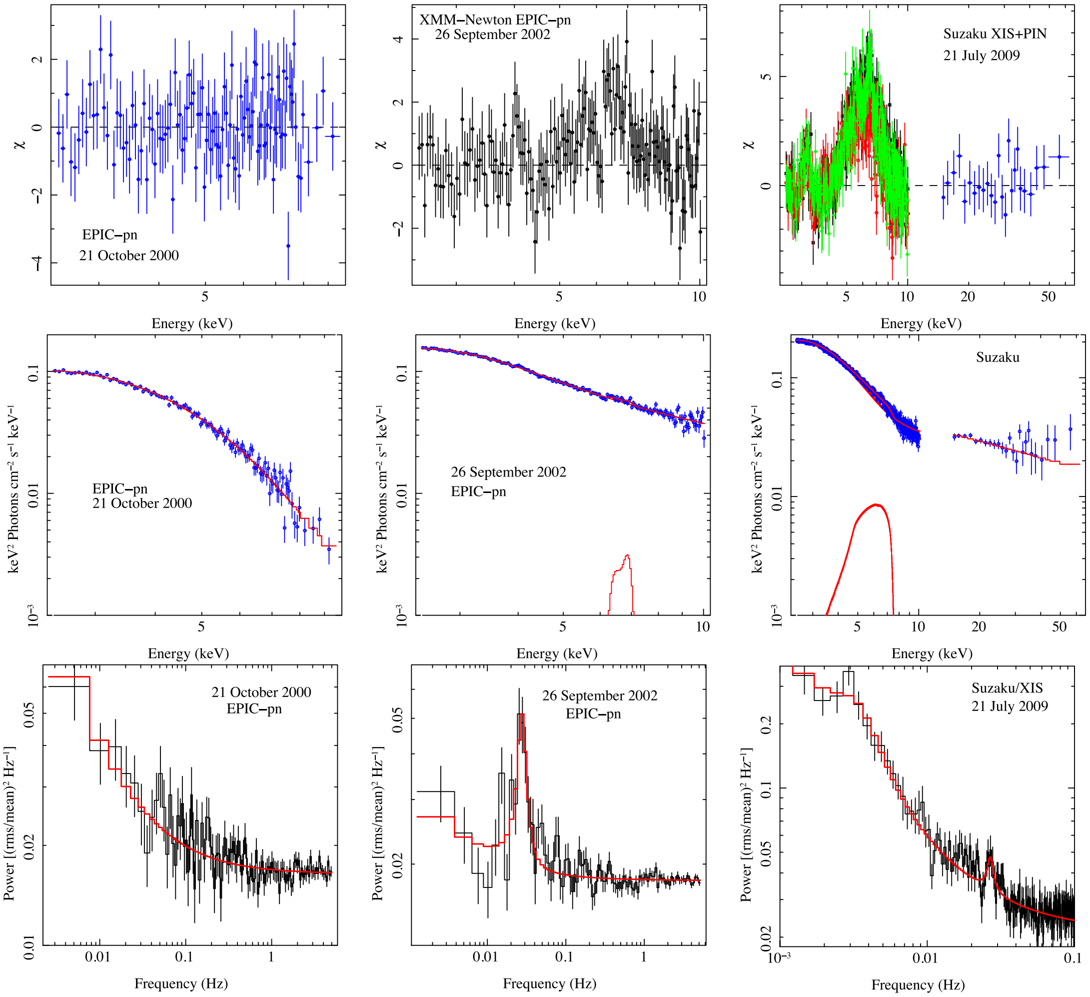

Figure 1. Results of spectral and temporal analysis of *Suzaku* and *XMM–Newton* observations of LMC X-1. Top panels: deviations of the observed *XMM–Newton* EPIC-pn XMM-101, XMM-401 and *Suzaku* XIS+PIN spectral data from the best-fitting TBVARABS×(DISKBB + SIMPL) models. Middle panels: unfolded EPIC-pn XMM-101, XMM-101 and *Suzaku* XIS+PIN spectral data and the best-fitting models TBVARABS×(DISKBB + SIMPL) for XMM-101 and TBVARABS×(DISKBB + SIMPL + LAOR) for *Suzaku* and XMM-401 data. Bottom panels: the PDS and the best-fitting models for the XMM-101, XMM-401 and *Suzaku*/XIS data.

Table 1. Best-fitting model parameter PDS derived from the *XMM–Newton* observations XMM-401 and XMM-101, and *Suzaku*.

Model	Parameter	XMM-401	XMM-101	*Suzaku*/XIS
		CONST. + QPO	CONST + PLAW[a]	CONST. + PLAW[a] + LO + QPO
CONSTANT		$0.0180^{+0.0002}_{-0.0004}$	0.0164 ± 0.0003	$0.0212^{+0.0002}_{-0.0007}$
PLAW	index	$-0.7^{+0.4}_{-3.3}$	$-0.85^{+0.14}_{-0.16}$	$-1.09^{+0.11}_{-0.04}$
	Norm (10^{-4})	$1.15^{+5.25}_{-1.11}$	$4.8^{+3.6}_{-2.4}$	$2.1^{+1.5}_{-0.2}$
LO	ν_L (10^{-3} Hz)	–	–	$3.1^{+0.5}_{-0.7}$
	FWHM	–	–	$3.1^{+2.8}_{-1.7}$
	Norm (10^{-4})	–	–	$4.4^{+1.7}_{-1.7}$
QPO	$\nu_{\rm qpo}(10^{-2}$ Hz)	$2.77^{+0.13}_{-0.12}$	–	$2.67^{+0.07}_{-0.06}$
	Q	$3.8^{+3.2}_{-1.4}$	–	$9.4^{+8.8}_{-5.0}$
	rms	$0.019^{+0.004}_{-0.003}$	–	$0.008^{+0.002}_{-0.002}$
	$\chi^2_{\rm min}$/dof	91.2/86	106.3/106	671.8/503
	$\Delta\chi^2$ (QPO)	−42.0	–	−23.0

[a]plaw: power-law model.

below 2.5 keV and used the XIS data in the 2.5–10 keV band. The broad iron line is clearly seen in the 4–7 keV band. There are also slight cross-calibration problems at a level of 2σ–3σ between the back-illuminated CCDs (XIS0 and XIS3) and the front-illuminated CCD (XIS1) in the iron K band. We added a 1 per cent systematic error to each of the three XIS data sets to account for possible uncertainties in the calibration of different instruments. We grouped the PIN data to a minimum signal-to-noise of 3 per bin and used the 15–70 keV band. We fitted the XIS and PIN data jointly with the absorbed DISKBB and the empirical convolution model of Comptonization SIMPL which gives the fraction of photons in the input seed spectrum that are upscattered into a power-law component (Steiner et al. 2009). Since SIMPL redistributes seed photons to higher energies, we extended the sampled energies to 1000 keV to calculate the model. We multiplied the model with a CONSTANT component to account for variations in the relative normalization of the instruments. The constant was fixed at 1 for XIS0 and 1.16 for PIN, and varied for XIS1 and XIS3. This model (model A: TBVARABS×(DISKBB∗SIMPL)) resulted in $\chi^2 = 1768.9$ for 736 degrees of freedom (dof). The fit is poor due to the presence of a broad feature in the 4.5–7 keV band reminiscent of relativistic iron Kα line. To show the broad iron line clearly, we excluded the data in the 4.5–8 keV band and refitted. This resulted in $\chi^2/\mathrm{dof} = 355.2/372$ with $N_{\mathrm{H}} \sim 9.6 \times 10^{21}\,\mathrm{cm}^{-2}$, $\Gamma \sim 2.36$ and $f_{\mathrm{scr}} \sim 0.12$. We then evaluated the best-fitting model in the 4.5–8 keV band. The upper-right panel in Fig. 1 shows the deviations of the observed data from the continuum model. To model the relativistic iron line, we added a LAOR line (model B: TBVARABS×(DISKBB∗SIMPL + LAOR)). The LAOR model describes the line profile from an accretion disc around a spinning black hole. We fixed the disc inclination at 36°.38 as determined by Orosz et al. (2009) based on optical and near-IR observations. We also fixed the outer radius to $r_{\mathrm{out}} = 400r_{\mathrm{g}}$ and constrained the line energy to vary between 6.4 and 6.9 keV. The fit resulted in $\chi^2/\mathrm{dof} = 839.6/731$ with $r_{\mathrm{in}} \sim 2.3r_{\mathrm{g}}$ and the line energy pegged to the highest allowed value possibly due to the presence of iron Kβ line. Since the broad iron line is thought to be the result of the blurred reflection from a disc, we replaced the LAOR model with REFLIONX model which describes the reflection from a partially ionized accretion disc with constant density as a result of the illumination of X-ray power-law emission from the corona (Ross, Fabian & Young 1999; Ross & Fabian 2005). We fixed the iron abundance at solar, and tied the photon indices of the illuminating power-law and the SIMPL Comptonization model. We then blurred the disc reflection with the convolution model KDBLUR to account for the Doppler and gravitational redshifts. As before, we fixed the inclination to $i = 36°.38$ and outer radius to $r_{\mathrm{out}} = 400r_{\mathrm{g}}$. This model (model C: TBVARABS×(DISKBB∗SIMPL + KDBLUR∗REFLIONX)) provided a good fit with $\chi^2/\mathrm{dof} = 765.6/731$. We have listed the best-fitting parameters for both models B and C in Table 2. Thus, we confirm the broad iron line earlier detected by Steiner et al. (2012) and obtained broadly similar iron line parameters though they used a more physical accretion disc and blurred reflection models and also accounted for reflection from the stellar wind by using an ionized reflection model.

We have also analysed the timing mode EPIC-pn spectral data extracted from the two *XMM–Newton* observations. We grouped the EPIC-pn spectral data using the SAS task *specgroup* to ensure a minimum of 20 counts per bin and at most 5 bins in a full width at half-maximum (FWHM) resolution. First, we used the DISKBB model modified by neutral absorption (TBVARABS). As before, we fixed the abundances as obtained by Hanke et al. (2010). The absorbed DISKBB model fitted to the XMM-101 EPIC-pn spectral data resulted in $\chi^2/\mathrm{dof} = 125/109$ with $N_{\mathrm{H}} < 1.5 \times 10^{21}\,\mathrm{cm}^{-2}$ and $kT_{\mathrm{in}} = 0.928 \pm 0.007$ keV. The absorption column inferred from the TBVARABS×DISKBB model was at least a factor of 5 lower than that derived for the *Suzaku* data. Including the SIMPL component (model A) resulted in $N_{\mathrm{H}} < 0.7 \times 10^{22}\,\mathrm{cm}^{-2}$ and improved the fit marginally to $\chi^2/\mathrm{dof} = 115.8/107$ which corresponds to 98.3 per cent confidence level according to an *F*-test. The best-fitting scattering fraction, $f_{\mathrm{pl}} = 0.026^{+0.014}_{-0.021}$, indicates that the Comptonizing component was extremely weak in the XMM-101 observation.

For XMM-401, the absorbed DISKBB model resulted in a statistically unacceptable fit ($\chi^2/\mathrm{dof} = 5629.6/156$) due to the presence of a hard component. Use of the Comptonization model SIMPL (model A) improved the fit ($\chi^2/\mathrm{dof} = 169.4/154$). Careful examination of the fit residuals showed a hint of broad iron line. We excluded the 5–8 keV band, performed the fitting and compared the observed data with the continuum model. We added the LAOR line with the emissivity index fixed at $q = 3$. Model B improved the fit ($\Delta\chi^2 = -23.9$ for three parameters). We also calculated 1σ error on the line flux and found that the broad iron line is detected at a 3.3σ level. Next, we replaced the LAOR line with REFLIONX convolved with KDBLUR (model C) with emissivity index fixed at $q = 3$. This model also resulted in a good fit ($\chi^2/\mathrm{dof} = 142.2/151$). The best-fitting parameters are listed in Table 2. For the *Suzaku* and XMM-401 data, the best-fitting equivalent hydrogen column density is in the range of 0.8–1.8 $\times 10^{22}\,\mathrm{cm}^{-2}$ while for the XMM-101 data, we could only obtain the 90 per cent upper limit ($N_{\mathrm{H}} < 0.7 \times 10^{22}\,\mathrm{cm}^{-2}$). These values are generally consistent with earlier measurements. Using six soft X-ray spectra obtained with grating and/or CCD, Hanke et al. (2010) measured $N_{\mathrm{H}} = (1\text{–}1.3) \times 10^{22}\,\mathrm{cm}^{-2}$ for the DISKBB∗SIMPL model and $N_{\mathrm{H}} = (1\text{–}2) \times 10^{22}\,\mathrm{cm}^{-2}$ for the DISKBB×POWERLAW model, with a systematic dependence on the orbital phase. Earlier measurements with *Chandra*, *BeppoSAX*, *ASCA* and *BBXRT* span a range of 4.4–8.6 $\times 10^{21}\,\mathrm{cm}^{-2}$ (see table 2 in Orosz et al. 2009).

5 DISCUSSION AND CONCLUSIONS

We have performed power and energy spectral study of the persistent BHB LMC X-1. The PDS shape of LMC X-1 as measured with *XMM–Newton* and *Suzaku* is approximately a power law ($P \propto \nu^{\alpha}$; $\alpha \sim -1$), with rms variability of 4.3 per cent (XMM-101), 2.7 per cent (XMM-401) and 4.2 per cent (*Suzaku*) in the 10^{-3}–1 Hz range. These values are generally consistent with earlier measurements by *Ginga* (Ebisawa et al. 1989), *RXTE* (e.g. Wilms et al. 2001) and typical of an HSS. We have discovered QPOs from LMC X-1 at around 27 mHz in *XMM–Newton* (XMM-401) and *Suzaku* observations. These QPOs appear to be remarkable as their centroid frequencies are very low compared to that of type A, B or C QPOs observed from black hole transients in out]. Additionally, they appear in the HSS when QPOs are usually not observed.

The quality factors of these QPOs ($Q \sim 4$ for XMM-401, ~10 for *Suzaku* data) are comparable to that of type B or C QPOs, and the rms (~1.1–1.7 per cent) are comparable to type A QPOs. However, the frequencies are much lower than that observed from type A and B QPOs, and the very low frequency type C QPOs are seen only in hard states, much different from what we observe here.

There are very few QPOs from the persistent and wind-fed BHB. In the case of LMC X-1, Ebisawa et al. (1989) claimed detection of QPOs at 75 and 142 mHz with 2.9 and 1.8 per cent rms, respectively, based on *Ginga* observations. The weaker QPO is likely to be the second harmonic. Thus, the frequencies of the QPOs discovered with *Ginga* are higher but the rms of these QPOs are within the range

Table 2. Best-fitting spectral parameters of LMC X-1 derived from the *XMM–Newton* and *Suzaku* observations.

Component	Parameter$^{(a)}$	*Suzaku*		XMM-401		XMM-101
		Model B$^{(b)}$	Model C$^{(b)}$	Model B$^{(b)}$	Model C$^{(b)}$	Model A$^{(b)}$
TBVARABS	$N_{\rm H}$ (10^{22} cm^{-2})	$1.08^{+0.24}_{-0.24}$	$1.66^{+0.15}_{-0.18}$	$1.0^{+0.3}_{-0.2}$	$1.1^{+0.4}_{-0.2}$	<0.7
DISKBB	$kT_{\rm in}$ (keV)	$0.79^{+0.02}_{-0.01}$	$0.77^{+0.02}_{-0.01}$	0.65 ± 0.02	0.68 ± 0.01	0.90 ± 0.03
	$n_{\rm diskbb}{}^{(c)}$	$96.4^{+12.9}_{-6.7}$	$101.7^{+18.9}_{-9.1}$	172^{+72}_{-51}	$133.8^{+4.7}_{-5.8}$	$23.8^{+5.3}_{-2.5}$
SIMPL	Γ	$2.45^{+0.04}_{-0.04}$	$2.41^{+0.06}_{-0.04}$	$2.91^{+0.04}_{-0.13}$	$2.80^{+0.04}_{-0.06}$	3.3^{+p}_{-p}
	$f_{\rm scr}$	$0.138^{+0.004}_{-0.005}$	$0.078^{+0.014}_{-0.017}$	$0.35^{+0.02}_{-0.04}$	$0.294^{+0.019}_{-0.008}$	$0.026^{+0.014}_{-0.021}$
REFLIONX	$n_{\rm ref}^{(d)}$ ($\times 10^{-7}$)	–	$1.17^{+0.22}_{-0.16}$	–	$4.5^{+p}_{-3.6}$	–
	Fe/solar	–	1 (f)	–	1 (f)	–
	ξ (erg cm s^{-1})	–	>8360	–	1795^{+1042}_{-770}	–
KDBLUR	i	–	36°.38 (f)	–	36°.38 (f)	–
	$r_{\rm in}$ ($r_{\rm g}$)	–	$2.38^{+0.59}_{-0.19}$	–	>32	–
	$r_{\rm out}$ ($r_{\rm g}$)	–	400 (f)	–	400 (f)	–
	q	–	$3.37^{+0.25}_{-0.19}$	–	3 (f)	–
LAOR	$E_{\rm line}$ (keV)	$6.9^{+p}_{-0.02}$	–	$6.69^{+0.11}_{-0.10}$	–	–
	$r_{\rm in}$	$2.3^{+0.1}_{-0.1}$	–	64^{+113}_{-31}	–	–
	$r_{\rm out}$ ($r_{\rm g}$)	400 (f)	–	400 (f)	–	–
	q	$4.5^{+0.1}_{-0.1}$	–	3 (f)	–	–
	$f_{\rm line}^{(e)}$	$7.9^{+1.1}_{-1.0} \times 10^{-4}$	–	$4.6^{+1.7}_{-2.0} \times 10^{-5}$	–	–
	$\chi^2_{\rm min}$/dof	839.6/731	765.6/731	145.5/151	145.2/151	115.8/107
	$f_{2.5-10\,{\rm keV}}^{(f)}$	2.4×10^{-10}	2.4×10^{-10}	2.0×10^{-10}	2.0×10^{-10}	1.0×10^{-10}
	$f_{10-60\,{\rm keV}}^{(f)}$	7.8×10^{-11}	7.8×10^{-11}	–	–	–
	disc frac.$^{(g)}$	∼0.60	–	∼0.35	–	∼94

(*a*) p indicates that the error calculations pegged at the lower/upper bounds and (f) indicates a fixed parameter.
(*b*) Models A: TBVARABS×DISKBB∗SIMPL; B: TBVARABS×(DISKBB∗SIMPL + LAOR); C: TBVARABS×(DISKBB∗SIMPL + KDBLUR∗REFLIONX).
(*c*) DISKBB normalization $n_{\rm diskbb} = (\frac{R_{\rm in}/{\rm km}}{D/10{\rm kpc}})^2 \cos i$, where $R_{\rm in}$ is an apparent inner radius, D is the distance and i is the inclination angle.
(*d*) REFLIONX normalization in units of photons cm^{-2} s^{-1}keV^{-1} at 1 keV.
(*e*) Flux of the LAOR line in units of photons cm^{-2} s^{-1}.
(*f*) Observed flux in units of erg cm^{-2} s^{-1}.
(*g*) Fraction of disc flux and the SIMPL flux in the 2–20 keV.

of those measured with *XMM–Newton* and *Suzaku* observations. It is likely that all these QPOs are similar in nature but vary in their peak frequencies.

The X-ray energy spectrum of LMC X-1 is dominated by two spectral components – accretion disc blackbody and a Comptonizing component or a steep power law as was also noted earlier (see Ebisawa et al. 1989; Schlegel et al. 1994; Schmidtke et al. 1999; Gierliński, Maciołek-Niedźwiecki & Ebisawa 2001; Nowak et al. 2001; Wilms et al. 2001; Ruhlen, Smith & Swank 2011; Steiner et al. 2012). We have confirmed the broad, relativistic iron line from LMC X-1 in the *Suzaku* data, earlier studied in detail by Steiner et al. (2012) who measured the black hole spin parameter $a = 0.97^{+0.02}_{-0.25}$ (68 per cent range). We measure the inner radius to be $r_{\rm in} = 2.4^{+0.6}_{-0.2} r_{\rm g}$, which corresponds to a similar spin parameter though we used a simpler model. In addition, we also detected broad iron line in one of the *XMM–Newton* observation (XMM-401). However, the line was narrower ($r_{\rm in} > 32 r_{\rm g}$) and weaker by at least an order of magnitude compared to the relativistic line measured with the *Suzaku* data.

We did not detect an iron line in the XMM-101 observation. The 90 per cent upper limit on the flux of a LAOR line at 6.7 keV with $r_{\rm in} = 64 r_{\rm g}$ (similar to the line in the XMM-401 data) is 3.8×10^{-5} photons cm^{-2} s^{-1}. This 90 per cent limit on the iron-line flux is nearly two orders of magnitude lower than the line flux measured in the *Suzaku* data but it is formally consistent with the 90 per cent range measured with the XMM-401 data. In any case, the iron line from LMC X-1 is variable and is only detected clearly when a strong power-law component is present.

We have also found strong variability of the power-law component in the energy spectrum. In the first *XMM–Newton* observation (XMM-101), the power-law component is almost absent. In this observation, the fraction of the disc emission in the 2–20 keV was ∼94 per cent and LMC X-1 was in the soft state. In the second *XMM–Newton* (XMM-401) and the *Suzaku* observations, the power-law component was very strong with disc fractions ∼35 and ∼60 per cent, respectively, in the 2–20 keV band (see Table 2). The spectral variability of LMC X-1 is also well studied. Schmidtke et al. (1999) showed that spectral variability of LMC X-1 mainly arises from the changes in the intensity of the high-energy power-law component.

The clear presence of the broad iron line as well as the QPOs in the X-ray emission from LMC X-1 appears to depend on the presence of a strong power-law component.

The QPOs must arise from the inner regions where substantial X-ray variability is produced. Indeed, there are theoretical models that show oscillations in the inner regions of accretion discs.

Titarchuk & Osherovich (2000) have shown that the very low frequency QPOs in both BHB and neutron star X-ray binaries are caused by global disc oscillations in the direction normal to the disc. They argue that these disc oscillations are the result of gravitational interaction between the compact object and the accretion disc. The frequency of the global disc oscillations can be written as

$$\nu_0 \approx 2\left(\frac{R_{\rm in}}{3R_{\rm S}}\right)^{-\frac{8}{15}}\left(\frac{M_{\rm BH}}{\rm M_{\odot}}\right)^{-\frac{8}{15}}\left(\frac{P_{\rm orb}}{3\,\rm h}\right)^{-\frac{7}{15}}\left(\frac{R_{\rm adj}}{R_{\rm in}}\right)^{-0.3}\ \rm Hz \qquad (1)$$

(Titarchuk & Osherovich 2000). Using $P_{\rm orb} = 3.9$ d, $M_{\rm BH} = 10.9\,\rm M_{\odot}$ (Orosz et al. 2009), $R_{\rm in} = 2.3R_{\rm g}$ from the broad iron-line fit to the *Suzaku* data (see Table 2), and the adjustment radius $R_{\rm adj} = 2R_{\rm in}$ (Titarchuk & Osherovich 2000), we find $\nu_0 \approx 0.15$ Hz. Thus, the global disc oscillations are ∼five times faster than the observed QPOs. Hence, the global mode oscillations are unlikely to explain the observed QPOs from LMC X-1.

Very low frequency QPOs in the mHz range have been observed from BHBs, e.g. the dynamic QPOs in the 1 mHz–10 Hz range changing their frequency on minutes (Morgan et al. 1997), the 'heartbeat' QPOs from GRS 1915+105 (Belloni et al. 2000) and IGR J17091−3624 (Altamirano et al. 2011a). The millihertz heartbeat QPOs from GRS 1915+105 and IGR J17091−3624 occur during the high-luminosity, soft states and are thought to be due to limit-cycle oscillations of local accretion rate in the inner disc (Neilsen, Remillard & Lee 2011). The millihertz QPOs from LMC X-1 are also detected in the high luminosity (∼$0.5L_{\rm Edd}$) with strong soft component. However, the scattering fraction ($f_{\rm SC} \gtrsim 0.13$–1; Neilsen et al. 2011) of GRS 1915+105 during the heartbeat oscillation appears to be higher than the averaged scattering fraction $f_{\rm SC} \sim 0.1$ we found in the presence of QPO for LMC X-1. Also, rms amplitude of the QPOs from LMC X-1 is low (1–2 per cent) compared to the rms amplitude of the heartbeat QPOs from GRS 1915+105, though the amplitude can be as low as ∼3 per cent in the case of IGR J17091-3624 (see e.g. Altamirano et al. 2011b). Moreover, the heartbeat oscillations in the ρ and μ classes of GRS 1915+105 and IGR J17091−3624 generally depict a peculiar pattern – slow rise and fast decay with changes in the count rates by factors ∼2–5 (e.g. Belloni et al. 2000; Altamirano et al. 2011a; Rao & Vadawale 2012). Though it is difficult to infer the pattern of individual variability events, such large amplitude variability is not seen in the light curves of LMC X-1. Thus, the mHz QPOs from LMC X-1 are unlikely to be the 'heartbeat' QPOs.

Very low frequency, 'non-heartbeat' oscillations have also been found in BHBs. Altamirano & Strohmayer (2012) have reported 11 mHz QPOs from the black hole candidate H 1743−322 in its successive outbursts eight months apart. These QPOs were almost constant in their peak frequency and were detected in the LHS state of H 1743−322. Given the differences in the spectral states and luminosity of LMC X−1 and H 1743−322, it is likely that the QPOs from these two sources arise from different physical phenomena.

The QPOs we detected from LMC X-1 are in the same frequency range as those observed in some ULXs, whereas there are attempts to identify them in order to scale with mass. If these are the same features, ULXs would host a black hole of a few solar masses. The mHz QPOs from LMC X-1 are the only LFQPOs from any persistent, wind-fed BHB. A detailed study of these QPOs and their dependence on energy, broad-band energy spectral and PDS shape, and absorption will be required to investigate their nature. The variable nature of these QPOs and the broad iron line from LMC X-1 possibly related to strength of the power-law component can be used to study the disc–corona coupling and the origin of both these features. The *ASTROSAT* mission, scheduled to launch in a year, is well suited for detailed study of these QPOs.

ACKNOWLEDGEMENTS

We thank an anonymous referee for useful comments and suggestions. The authors thank M. A. Nowak, R. Misra and A. R. Rao for discussion on this work. TMB acknowledges support from grant INAF PRIN 2012-6. This research has made use of the General High-energy Aperiodic Timing Software (GHATS) package developed by T. M. Belloni at INAF – Osservatorio Astronomico di Brera. TMB and GCD acknowledge support from the joint Indo-Italian project, grant IN12MO12, by the Department of Science and Technology (DST), India and the Ministry of External Affairs, Italy. This work is based on observations obtained with *XMM–Newton*, an ESA science mission with instruments and contributions directly funded by ESA Member States and the USA (NASA). This research has made use of data obtained from the High Energy Astrophysics Science Archive Research Center (HEASARC), provided by NASA's Goddard Space Flight Center. SJ and GCD acknowledge support from grant under ISRO-RESPOND programme (ISRO/RES/2/384/2014-15).

REFERENCES

Altamirano D., Strohmayer T., 2012, ApJ, 754, L23
Altamirano D. et al., 2011a, ApJ, 742, L17
Altamirano D. et al., 2011b, Astron. Telegram, 3225, 1
Belloni T. M., 2010, in Belloni T., ed., Lecture Notes in Physics, Vol. 794, The Jet Paradigm. Springer-Verlag, Berlin, p. 53
Belloni T., Hasinger G., 1990, A&A, 230, 103
Belloni T., van der Klis M., Lewin W. H. G., van Paradijs J., Dotani T., Mitsuda K., Miyamoto S., 1997, A&A, 322, 857
Belloni T., Klein-Wolt M., Méndez M., van der Klis M., van Paradijs J., 2000, A&A, 355, 271
Belloni T. M., Motta S. E., Muñoz-Darias T., 2011, Bull. Astron. Soc. India, 39, 409
Belloni T. M., Sanna A., Méndez M., 2012, MNRAS, 426, 1701
Caballero-García M. D., Belloni T., Zampieri L., 2013, MNRAS, 436, 3262
Casella P., Belloni T., Homan J., Stella L., 2004, A&A, 426, 587
Casella P., Belloni T., Stella L., 2005, ApJ, 629, 403
Corbel S., Coriat M., Brocksopp C., Tzioumis A. K., Fender R. P., Tomsick J. A., Buxton M. M., Bailyn C. D., 2013, MNRAS, 428, 2500
Cowley A. P., Schmidtke P. C., Anderson A. L., McGrath T. K., 1995, PASP, 107, 145
Dewangan G. C., Titarchuk L., Griffiths R. E., 2006, ApJ, 637, L21
Dheeraj P. R., Strohmayer T. E., 2012, ApJ, 753, 139
Ebisawa K., Mitsuda K., Inoue H., 1989, PASJ, 41, 519
Gierliński M., Maciołek-Niedźwiecki A., Ebisawa K., 2001, MNRAS, 325, 1253
Gou L. et al., 2009, ApJ, 701, 1076
Hanke M., Wilms J., Nowak M. A., Barragán L., Schulz N. S., 2010, A&A, 509, L8
Lewin W. H. G., van der Klis M., 2006, Compact Stellar X-ray Sources. Cambridge Univ. Press, Cambridge
Markwardt C. B., Swank J. H., Taam R. E., 1999, ApJ, 513, L37
Miller J. M., 2007, ARA&A, 45, 441
Morgan E. H., Remillard R. A., Greiner J., 1997, ApJ, 482, 993
Motta S., Belloni T., Homan J., 2009, MNRAS, 400, 1603
Motta S., Muñoz-Darias T., Casella P., Belloni T., Homan J., 2011, MNRAS, 418, 2292
Mucciarelli P., Casella P., Belloni T., Zampieri L., Ranalli P., 2006, MNRAS, 365, 1123
Neilsen J., Remillard R. A., Lee J. C., 2011, ApJ, 737, 69

Nowak M. A., Wilms J., Heindl W. A., Pottschmidt K., Dove J. B., Begelman M. C., 2001, MNRAS, 320, 316
Orosz J. A. et al., 2009, ApJ, 697, 573
Pasham D. R., Strohmayer T. E., 2013, ApJ, 771, 101
Rao A., Vadawale S. V., 2012, ApJ, 757, L12
Remillard R. A., McClintock J. E., 2006, ARA&A, 44, 49
Remillard R. A., Morgan E. H., McClintock J. E., Bailyn C. D., Orosz J. A., 1999, ApJ, 522, 397
Reynolds C. S., Nowak M. A., 2003, Phys. Rep., 377, 389
Ross R. R., Fabian A. C., 2005, MNRAS, 358, 211
Ross R. R., Fabian A. C., Young A. J., 1999, MNRAS, 306, 461
Ruhlen L., Smith D. M., Swank J. H., 2011, ApJ, 742, 75
Schlegel E. M., Marshall F. E., Mushotzky R. F., Smale A. P., Weaver K. A., Serlemitsos P. J., Petre R., Jahoda K. M., 1994, ApJ, 422, 243
Schmidtke P. C., Ponder A. L., Cowley A. P., 1999, AJ, 117, 1292
Steiner J. F., Narayan R., McClintock J. E., Ebisawa K., 2009, PASP, 121, 1279
Steiner J. F. et al., 2012, MNRAS, 427, 2552
Strohmayer T. E., Mushotzky R. F., 2003, ApJ, 586, L61
Titarchuk L., Osherovich V., 2000, ApJ, 542, L111
Trudolyubov S. P., Borozdin K. N., Priedhorsky W. C., 2001, MNRAS, 322, 309
Wilms J., Allen A., McCray R., 2000, ApJ, 542, 914
Wilms J., Nowak M. A., Pottschmidt K., Heindl W. A., Dove J. B., Begelman M. C., 2001, MNRAS, 320, 327

This paper has been typeset from a TEX/LATEX file prepared by the author.